Wheel-rail dynamic interaction

Yang, Zhen; Li, Zili

Citation (APA)
Yang, Z., & Li, Z. (2022). Wheel-rail dynamic interaction. In R. Calçada, & S. Kaewunruen (Eds.), *Rail Infrastructure Resilience: A Best-Practices Handbook* (pp. 111-135). Elsevier. https://doi.org/10.1016/B978-0-12-821042-0.00004-6

Important note
To cite this publication, please use the final published version (if applicable).
Please check the document version above.

Wheel-rail dynamic interaction 7

Zhen Yang and Zili Li
Delft University of Technology, Delft, The Netherlands

7.1 Introduction

7.1.1 Wheel-rail contact vs wheel-rail dynamic interaction

When a railway wheel rolls along a straight rail without significant geometric or stiffness irregularity, wheel-rail contact can be modeled analytically [1–4] or with a boundary element method (BEM) [5] based on the assumptions of half-space and linear elasticity. The analyzing scope of the contact problem is then concentrated on the potential contact region, as indicated by the red frame in Fig. 7.1A. When a wheel passes a more complex section of the track, e.g., a sharp curve, rail joint, or turnout, arbitrary contact geometry, and plastic deformation may occur, and the wheel-rail contact is generally better to be modeled with a finite element method (FEM) [6–19], in which arbitrary contact geometries and material nonlinearities can be handled. By discretizing the structures of interest in the spatial domain, the stresses/strains, deformation, and motion of the whole wheel and rail structures can be analyzed, as shown in Fig. 7.1B. In contrast to "wheel-rail contact" where only a local contact region is of concern, the term "wheel-rail interaction" denotes that the behavior of wheel and rail structures with certain geometric and material properties contribute to and are influenced by wheel-rail contact.

Early finite element (FE) studies on the wheel-rail interaction generally assumed quasistatic-state contact [7,8,11]; however, when a wheel passes complex sections of the track, dynamic effects often play a significant role in the wheel-rail interaction. Here the dynamic effects denote that the inertia of wheel/rail material influences the stress field in and surrounding the contact area, as well in the structure; the contact-induced wheel/rail structural vibration may significantly affect the wheel-rail contact [10,14,16–18]. Wheel-rail dynamic interaction should thus be considered, as schematically indicated in Fig. 7.1C. The explicit FEM is an ideal approach to deal with wheel-rail dynamic interaction, owing to its capabilities of handling nonlinear material properties and arbitrary contact geometries and considering dynamic effects [18] (to be elaborated and demonstrated in Section 7.2).

7.1.2 Weak spots of the track

The aforementioned complex track sections where wheel-rail dynamic interaction often occurs can be roughly categorized as the impact-inducing sections and the large-friction-inducing sections. For both, large wheel-rail contact force in the normal or/and tangential directions can be expected, consequently causing high-amplitude
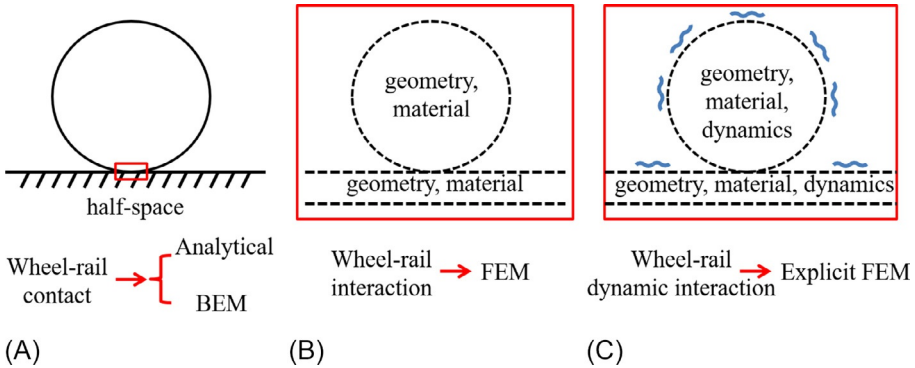
Rail Infrastructure Resilience. https://doi.org/10.1016/B978-0-12-821042-0.00004-6
Copyright © 2022 Elsevier Inc. All rights reserved.

Fig. 7.1 From wheel-rail contact to the dynamic interaction (A) wheel-rail contact; (B) wheel-rail interaction; (C) wheel-rail dynamic interaction.
Reproduced from Z. Yang, Numerical Modelling of Wheel-Rail Dynamic Interactions With an Explicit Finite Element Method (PhD thesis), Delft University of Technology, 2018, https://doi.org/10.4233/uuid:8acb9b48-bf77-45b2-a0d6-1cf6658f749e.

structural vibration and noise, accelerating track degradation. These complex sections can thus be regarded as weak spots of the track.

Typical impact-inducing track sections include rail joints and turnouts. When trains pass over these sections, wheel-rail impacts are generated due to the track stiffness and geometric irregularities. The impact, besides leading to vibration and noise, initiates and accelerates track deterioration, e.g., squat, plastic deformation, corrugation, fastening failure, hanging sleepers, and uneven track settlement. The impact-inducing track sections contribute to a large portion of the maintenance and renewal costs of the track infrastructure. For example, the impact load at a turnout can be more than two times the static wheel-rail contact load in amplitude, resulting in eight unexpectedly broken frog points per week in the Netherlands.

The large-friction-inducing sections include curves and places where acceleration and braking frequently take place. When a train negotiates a tight curve, large lateral friction force occurs at the contact between the tread of the inner wheel and the top surface of the low rail, and between the flange of the outer wheel and the gauge corner of the high rail, if a wheelset fails to align itself tangentially to the rail. The large friction force may induce full slip and stick-slip contact behavior and, consequently, severe wear, rolling contact fatigue, corrugation, and squeal noise. The flange contact introduces large spin creepage, causing severe wear and sometimes flange squeal. Large longitudinal friction force is generated in the acceleration and braking sections, as well as on slopes, where local wear of wheel tread (wheel flat) and railhead (wheel burn in a severe condition) may take place.

7.1.3   Consequences of the wheel-rail dynamic interaction

Based on the commonly-observed problems at the weak spots of the track, the consequences of the wheel-rail dynamic interaction can be summarized as the increased wheel/rail structure degradation and the contact-induced vibration and noise.

7.1.3.1 Wheel/rail structure degradation

Severe wear
Shown as the removal of material from the contacting surfaces of structures, wear is the most common failure mode of wheel/rail interface [20]. Severe wear is often observed at the gauge corner of the high rail on curves where flange contact takes place, as well as at the turnout noses and rail joints where impacts are generated. The worn profiles of wheel and rail further increase wheel-rail contact force and accelerate structure degradation.

Wheel polygonal wear, shown as periodic wave-like wear along the circumference of the wheel tread, commonly occurs in locomotives, metros, and high-speed trains. The dynamic effects play important roles in the generation of wheel polygon: the resonances of the train/track system are closely related to the wavelengths of the polygon [21–23].

Rolling contact fatigue
Rolling contact fatigue in the rail surface mainly includes squats and head checks. Squats mainly occur at welds, joints, turnouts, indentations, wheel burns, and corrugation, where wheel-rail impacts and excessive dynamic contact force are generated [10,14,19,24]. Squats in turn induce wheel-rail impacts. Head checks mainly occur on the curves with radii between 500 m and 3000 [25,26]. Rolling contact fatigue threatens the safety of railway traffic because the propagation of cracks may result in sudden rail fracture and derailment.

Corrugation
Corrugation comprises the formation of a periodic wave-shaped irregularity of the rail surface, and appears in almost all types of tracks, from ballast tracks to slab and embedded tracks, from heavy-haul to light rail and rapid transit [27,28]. The generation and development of corrugation can be explained by a short-term dynamic process and a long-term damage mechanism. The short-term dynamic process is believed to fix the wavelength of the periodic defect pattern to the dynamics of the train/track system, which is also the origin of the dynamic effects involved in the wheel-rail dynamic interaction. As to the long-term damage mechanism, the corrugation is considered to be formed by wear and plastic deformation.

7.1.3.2 Contact-induced vibration and noise

Impact vibration and noise
Impact vibration and noise are generated at the impact-inducing track sections. The vertical contact irregularities in the running surface generate high wheel-rail contact force and high-amplitude impact vibration and noise. The impact noise has discrete nature of the event, which can, however, be quite loud [29].

Friction induced vibration and squeal
Frictional induced unstable vibration of a railway wheel and the consequent squeal noise radiation often occur in sharp curves. The tonal squeal is one of the loudest and most disturbing railway noise sources. The wheel-rail dynamic interaction is

considered to be directly related to squeal generation [30,31]. Unsteady lateral creepage, particularly between the leading inner wheel and low rail, is thought to be the main cause of the unstable wheel vibration and curve squeal noise [29]. Flange contact has been found to reduce the likelihood of curve squeal due to lateral creepage under certain conditions [29], but may generate a different form of noise referred to as "flanging noise" or "flange squeal," which is much more broad-band in nature and also a source of considerable annoyance.

7.2   Modeling of wheel-rail dynamic interaction

Reliable modeling of wheel-rail dynamic interaction contributes to the mitigation and elimination of the aforementioned degradation and environmental impacts (i.e., vibration and noise), especially at the weak spots of the track. In addition, because the dynamic effects involved in wheel-rail interaction increase with the train speed and axle load, a better understanding of the wheel-rail dynamic interaction is necessary for the capacity increase of railway transportation.

7.2.1   Methodology

Owing to the capabilities of handling nonlinear material properties and arbitrary contact geometries and considering dynamic effects, the explicit FEM has been broadly employed to model wheel-rail dynamic interaction [10,13–18,28,31–35]. In comparison with the implicit FEM, the explicit integration scheme is more robust in handling difficult contact problems because it avoids the convergence difficulties caused by demanding contact conditions [36] and the regularization of the friction law required to treat the no-slip condition in the adhesion area [37]. Moreover, by avoiding the need for matrix evaluation, assembly, and decomposition as required by the implicit integration algorithms, the explicit procedure is computationally attractive for analyzing high-frequency dynamic problems of short-duration, especially when the total dynamic response time that must be modeled is only a few orders of magnitude longer than the stability critical time step, which is frequently the case in wave propagation analyses [38].

The core algorithms employed in the explicit FE wheel-rail dynamic interaction were systematically presented in [18]. Table 7.1 briefly presents the solution procedure of the explicit FEM that contains two loops. The outer loop is constructed mainly by formulating the equation of motion and solving the equation with the central difference scheme; and the inner loop calculates the wheel-rail contact, which is called as a subroutine at each time step prior to updating the structural dynamic responses. This solution procedure indicates that the calculation of wheel/rail dynamics and the calculation of wheel-rail frictional contact can be coupled in the numerical algorithm, and thus demonstrates that the explicit FEM is an ideal approach for the modeling of wheel-rail dynamic interaction.

Table 7.1 The solution procedure for the explicit FE wheel-rail dynamic interaction analysis.

Initialize algorithm: apply initial conditions; define contact pairs; construct the lumped mass
   matrix, and set the termination time
Loop 1: time step = 0, 1, 2, …
(I) Apply load conditions to construct the external force vector
(II) Process elements to construct the internal force vector
(III) Construct the wheel-rail contact force vector using the penalty contact method
   Loop 2: number of the node on the slave (wheel) surface = 1, 2, …
      (i) Locate the master (rail) segment for each slave (wheel) node
      (ii) Locate the wheel-rail contact points (projection of the slave node on the master
         segment)
      (iii) Calculate the contact force at the contact points
   END Loop 2
(IV) Update the nodal accelerations, velocities, and displacements using the central difference
   method
(V) Check for termination
END Loop 1
Output: wheel/rail nodal force and nodal motion (i.e., acceleration, velocity, and
   displacement)

7.2.2   Case studies

Three typical examples of using the explicit FEM to deal with wheel-rail dynamic
interaction are presented. The first example models the wheel-rail impact at a rail joint
[39]; the second and third examples deal with wheel-rail dynamic interaction at cur-
ves, i.e., frictional instability of the inter wheel [31] and flange contact of the outer
wheel [40], respectively.

7.2.2.1   Wheel-rail impacts at a rail joint

This example demonstrates the reliability of the explicit FEM for the modeling of
wheel-rail dynamic interaction. Because the explicit FEM couples the calculation
of wheel/rail dynamic responses with the calculation of wheel-rail contact (see
Table 7.1), the reliability of the wheel-rail dynamic interaction solutions are con-
firmed by separately validating the wheel/rail dynamic responses and contact
solutions.

A typical Dutch insulated rail joint (IRJ) without visible damage was selected as the
study target in the trunk line Amsterdam-Utrecht of the Dutch railway network. A 3D
explicit FE wheel-IRJ dynamic interaction model was built up, as shown in Fig. 7.2.
The model consists of a 10-m-long half-track with an IRJ in the middle and a half-
wheelset with the sprung mass of the car body and bogie. The ballast was simplified
as vertical spring and damper elements, with the displacements constrained in the lat-
eral and longitudinal directions. Since the stiffness and damping parameters used to
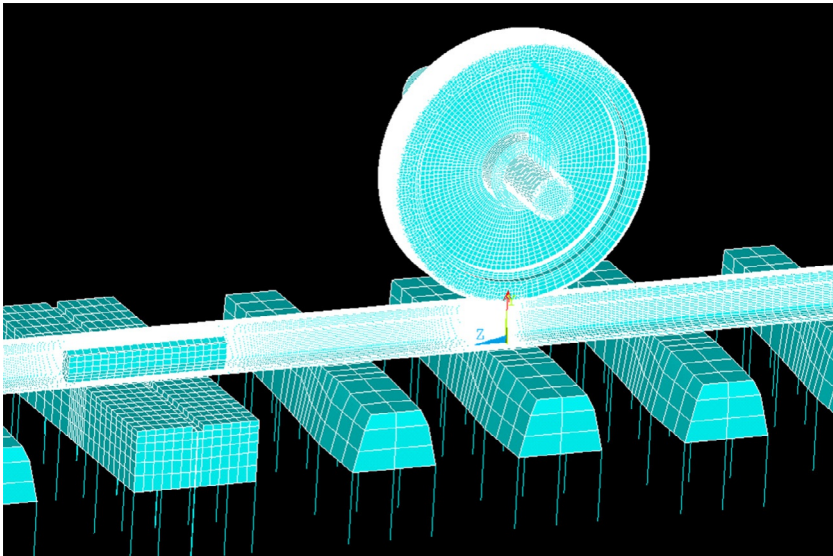
Fig. 7.2 A finite element wheel-IRJ dynamic interaction model.
Modified from Z. Yang, A. Boogaard, R. Chen, R. Dollevoet, Z. Li, Numerical and experimental study of wheel-rail impact vibration and noise generated at an insulated rail joint, Int. J. Impact Eng. 113 (2018) 29–39, https://doi.org/10.1016/j.ijimpeng.2017.11.008.

model the fastenings and ballast can hardly be measured directly in the field, these parameters were calibrated by fitting the simulated frequency response functions to the measurement results, which will be illustrated in detail in Section 7.3.1.

The simulated wheel-rail impact vibration response was validated against a trackside pass-by measurement. Fig. 7.3 compares the wavelet power spectra of the simulated (Fig. 7.3A) and measured (Fig. 7.3B–E) impact vibration up to 10 kHz. The results of the four pass-bys shown in Fig. 7.3 were successively measured when the four wheelsets of a coach passed the target IRJ. The simulated impact vibration agrees well with the pass-by measurement results in both the time domain and frequency domain. More details about the measurement campaign and model validation can be found in [39].

After validating the dynamic response, the simulated impact contact solutions are analyzed including the contact patch area, stress magnitude and direction, micro-slip, and adhesion-slip distributions. Detailed analyses and validation of the wheel-IRJ impact contact solutions can be found in [17]. By plotting a trail of transient contact areas, the "footprints" of the simulated contact patch are presented in Fig. 7.4A. Good correspondence can be obtained by comparing the simulated "footprints" to the in situ running band of the target IRJ shown in Fig. 7.4B, which implies that the simulation accurately reproduced the transient impact contact solutions.
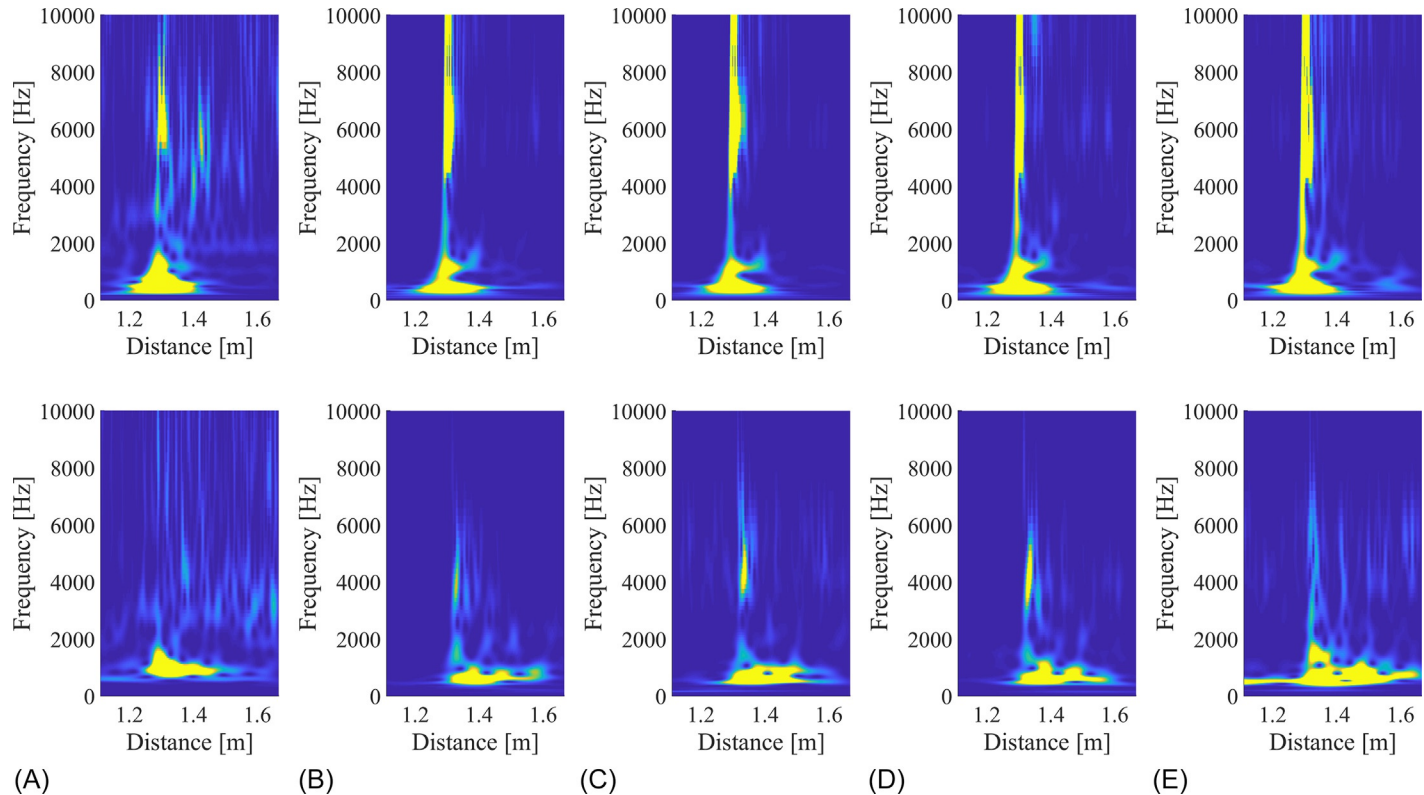
Fig. 7.3 Wavelet power spectra of the simulated and measured pass-by impact vibration. (Upper row: vertical impact vibration; lower row: lateral impact vibration; the unit of the color bar is m/s².) (A) Simulation; (B) 1st pass-by; (C) 2nd pass-by; (D) 3rd pass-by; (E) 4th pass-by.
Modified from Z. Yang, A. Boogaard, R. Chen, R. Dollevoet, Z. Li, Numerical and experimental study of wheel-rail impact vibration and noise generated at an insulated rail joint, Int. J. Impact Eng. 113 (2018) 29–39, https://doi.org/10.1016/j.ijimpeng.2017.11.008.
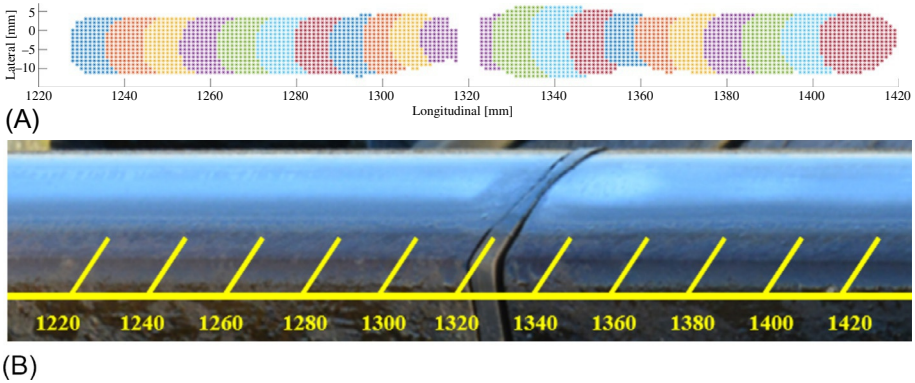
(A)

(B)

Fig. 7.4 Comparison of the simulated contact patch "footprints" and the in situ running band (A) "Footprints" of the simulated contact patch (the color differentiates an individual contact patch from the others); (B) in situ condition of the running band.

7.2.2.2 Frictional instability at curves

The second example simulates the curving behavior of the inner wheel to deal with the frictional instability, i.e., the squeal-exciting wheel-rail contact. The contact modeling accounting for the frictional instability of a vibrating wheel is considered the central part of the squeal prediction model [41]. Fig. 7.5 shows the employed 3D explicit FE wheel-rail, dynamic interaction model, with wheel lateral motion during curving. The wheel-rail contact was defined with nominal geometry and with the wheel flange being included. More detailed descriptions of the model can be found in [31].

In the simulation, the wheel rolled from its initial position at time t_0 to the solution zone along the rail, as shown in Fig. 7.5B. The dynamics arising from the wheel/rail initial kinematic and potential energy due to imperfect static equilibrium [13] have relaxed at time t_1. Wheel lateral motion was subsequently simulated from time t_2 by applying the prescribed displacement boundary conditions listed in Table 7.2 to both ends of the wheel half-axle, except for simulation case 1. The wheel entered the solution zone at time t_3 and exited at t_4. The dynamic evolution of the contact solutions was captured between t_3 and t_4.

Unsteady lateral creepage, particularly between the leading inner wheel and the low rail, is thought to be the main cause of squeal [29]. When simulating wheel lateral motion, the resulting wheel-rail lateral creepage causes asymmetric distributions of contact stress and micro-slip within the contact patch, as shown in Fig. 7.6. The asymmetry of the distribution of the contact patch is characterized by an orientation angle θ, as shown in Fig. 7.6C. The orientation angle increases with the lateral creepage from Fig. 7.6A–F. The orientation angles obtained with CONTACT [5] (4th row), are consistent with those obtained with the explicit FEM. The distributions of the adhesion-slip regions determined by the simulated explicit FE contact stresses in the 1st row and
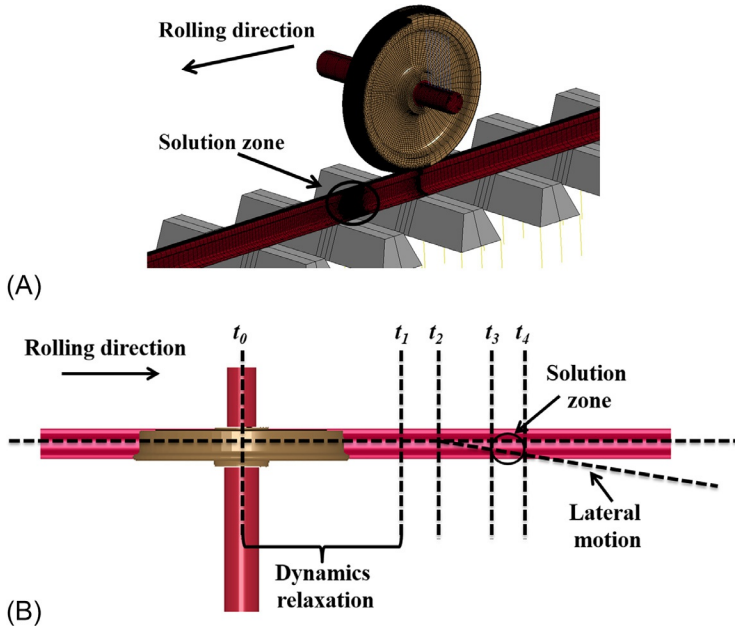
Fig. 7.5 The wheel-rail dynamic interaction model to simulate curving behavior (A) 3D FE model; (B) simulated frictional rolling with wheel lateral motion.
Reproduced with permission from Z. Yang, Z. Li, Numerical modeling of wheel-rail squeal-exciting contact, Int. J. Mech. Sci. 153–154 (2019) 490–499, https://doi.org/10.1016/j.ijmecsci.2019.02.012.

Table 7.2 Prescribed displacement boundary conditions applied to different simulation cases.

Prescribed displacement boundary conditions	Simulation cases
No lateral motion of the wheel	Case 1
Small lateral motion of the wheel	Case 2
Medium lateral motion of the wheel	Case 3
Large lateral motion of the wheel	Case 4

micro-slips in the 3rd row are in line with each other. They are also in reasonable agreement with the distributions of adhesion-slip regions determined by CONTACT in the 4th row. The main difference of the FE and boundary element (obtained with CONTACT) contact solutions is that the waves are observed in the micro-slip distributions calculated with the explicit FEM in Fig. 7.6E and F. The waves have been identified as the Rayleigh wave [42]. This confirms the transient/dynamic effects are included in the explicit FE contact modeling, which is needed for a correct representation of the squeal mechanisms [43].
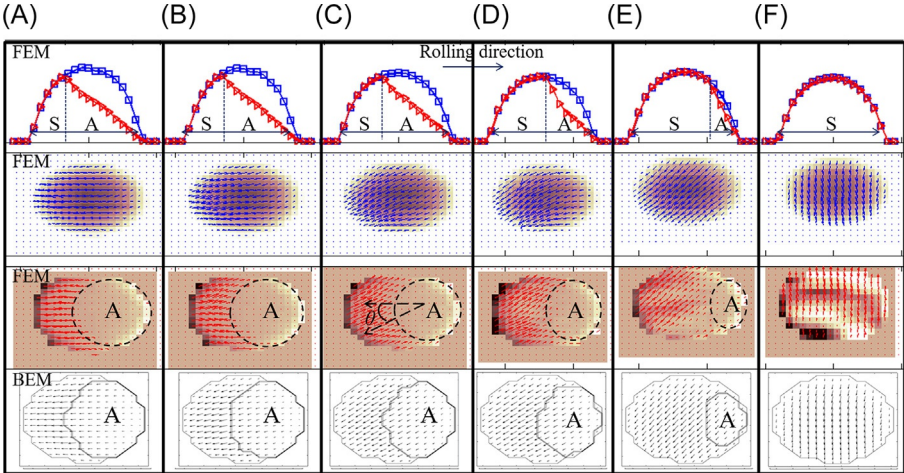
Fig. 7.6 Simulated contact solutions with lateral creepage. (1st row: stress distributions along the longitudinal centerline; 2nd row: stress distributions within the contact patch; 3rd row: micro-slip distributions within the contact patch; and 4th row: shear stress and adhesion-slip region distributions calculated with Kalker's CONTACT [5]. η and ξ are lateral and longitudinal creepage, respectively.) (A) simulation case 1 at 17.58 ms; (B) case 2 at 17.58 ms; (C) case 3 at 17.58 ms; (D) case 4 at 17.07 ms; (E) case 3 at 18.54 ms; and (F) case 4 at 17.94 ms. Reproduced with permission from Z. Yang, Z. Li, Numerical modeling of wheel-rail squeal-exciting contact, Int. J. Mech. Sci. 153–154 (2019) 490–499, https://doi.org/10.1016/j.ijmecsci.2019.02.012.

The time histories and power spectrum densities (PSDs) of the wheel dynamic lateral vibration calculated in simulation cases 1–4 are presented in Fig. 7.7A and B, respectively. The squeal-like vibration signals represented by large amplitude limit-cycles were produced when applying the wheel lateral motion. The amplitudes of the time histories increased with increasing amplitude of the lateral motion applied to the wheel model. Comparing the dominant frequencies of the vibration signals to the identified wheel modal frequencies, the wheel modes excited in the simulations can be determined: the mode with zero nodal circle and zero nodal diameter (0,0), the mode with zero nodal circle and three nodal diameters (0,3), and the mode with zero nodal circle and four nodal diameters (0,4), as detonated in Fig. 7.7B. The results correspond well to the conclusion that zero nodal circle modes tend to be excited in curve squeal [29].

7.2.2.3 Flanging and contact transition

The third example models nonsteady-state transition from single-point to two-point contact. The explicit FE wheel-rail dynamic interaction model presented in Section 7.2.2.2 (see Fig. 7.5A) was employed again but different boundary conditions were applied to the wheel in the manner shown in Fig. 7.8. The lateral displacement was constrained at the inner side of the wheel half-axle, and the outer end of the axle
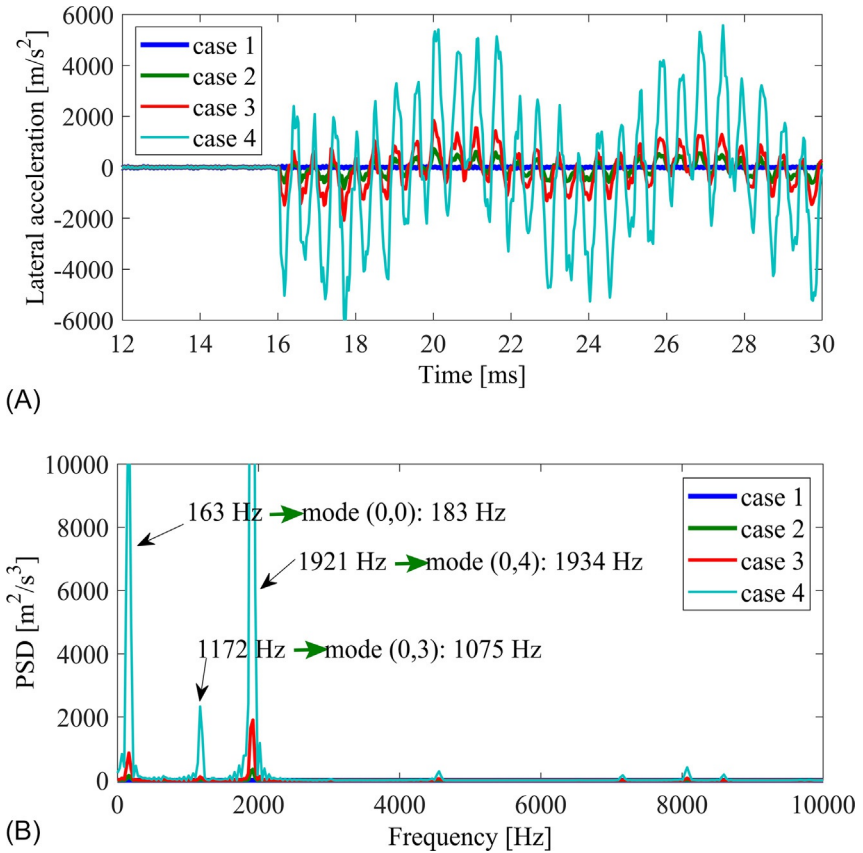
Fig. 7.7 Time histories and PSDs of the wheel lateral vibration simulated by different simulation cases. (A) Time histories; (B) PSDs.

was free. In the transient dynamic simulation, the wheel rolled from its initial position to the solution zone, forming an angle of attack (AoA) with respect to the rail longitudinal direction.

The contact transition is indicated by the simulated wheel-rail contact positions shown in Fig. 7.9. Initially, the wheel-rail contact occurred only between the rail top and wheel tread. A trail of blue patches represents the "footprints" of the single-point contact (Patch 1) in a series of time steps. Due to the presence of AoA, the wheel flange moved toward the gauge corner as the time step goes on and the 2nd contact patch (Patch 2) starts to appear. The "footprints" of the contact patches in the case of two-point contact are shown as two trails of red patches on the rail top and gauge corner.
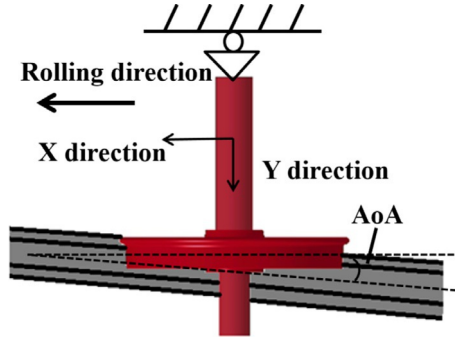
Fig. 7.8 Wheel-rail interaction model and the boundary conditions.
Reproduced with permission from Z. Yang, Z.L. Li, R. Dollevoet, Modelling of non-steady-state transition from single-point to two-point rolling contact, Tribol. Int. 101 (2016) 152–163, https://doi.org/10.1016/j.triboint.2016.04.023.

Fig. 7.9 Contact patches "footprints" (*blue* (*dark gray* in print version) for single-point contact and *red* (*light gray* in print version) for two-point contact).
Reproduced with permission from Z. Yang, Z.L. Li, R. Dollevoet, Modelling of non-steady-state transition from single-point to two-point rolling contact, Tribol. Int. 101 (2016) 152–163, https://doi.org/10.1016/j.triboint.2016.04.023.
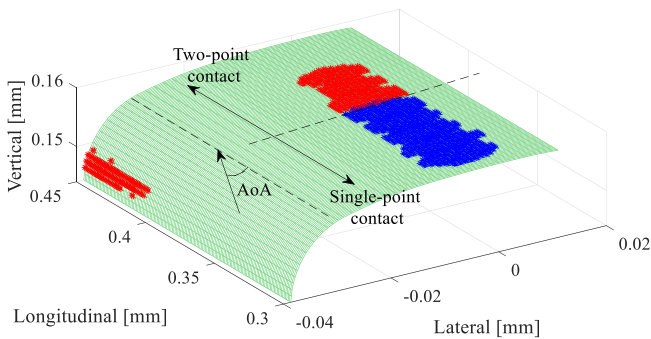
The evolution of the contact pressure and surface shear stress is plotted in the contour/vector diagrams in Figs. 7.10 and 7.11 for Patches 1 and 2, respectively. The pressure magnitude corresponds to the depth of color within the contact patch, as indicated by the color bar. It shows that the contact pressure and patch area decreases in Patch 1 but increases in Patch 2 once Patch 2 has arisen. The surface shear stresses in single-point and two-point contact are indicated by the blue and red arrows, respectively. The arrows point in the direction of the shear stress, and their lengths are proportional to the magnitudes. To characterize the direction of the surface shear stress, the orientation angle between the stress vector and the negative direction of the longitudinal axis is denoted as $\theta 1$ and $\theta 2$ in Patches 1 and 2, respectively. $\theta 1$ is typically small under a single-point contact, but it increases rapidly to approximately 90 degrees as the

Fig. 7.10 Evolution of pressure and surface shear stress distributions in Patch 1 (*blue color* (*dark gray* in print version) for shear stress indicates single-point contact; *red* (*light gray* in print version) indicates two-point contact).

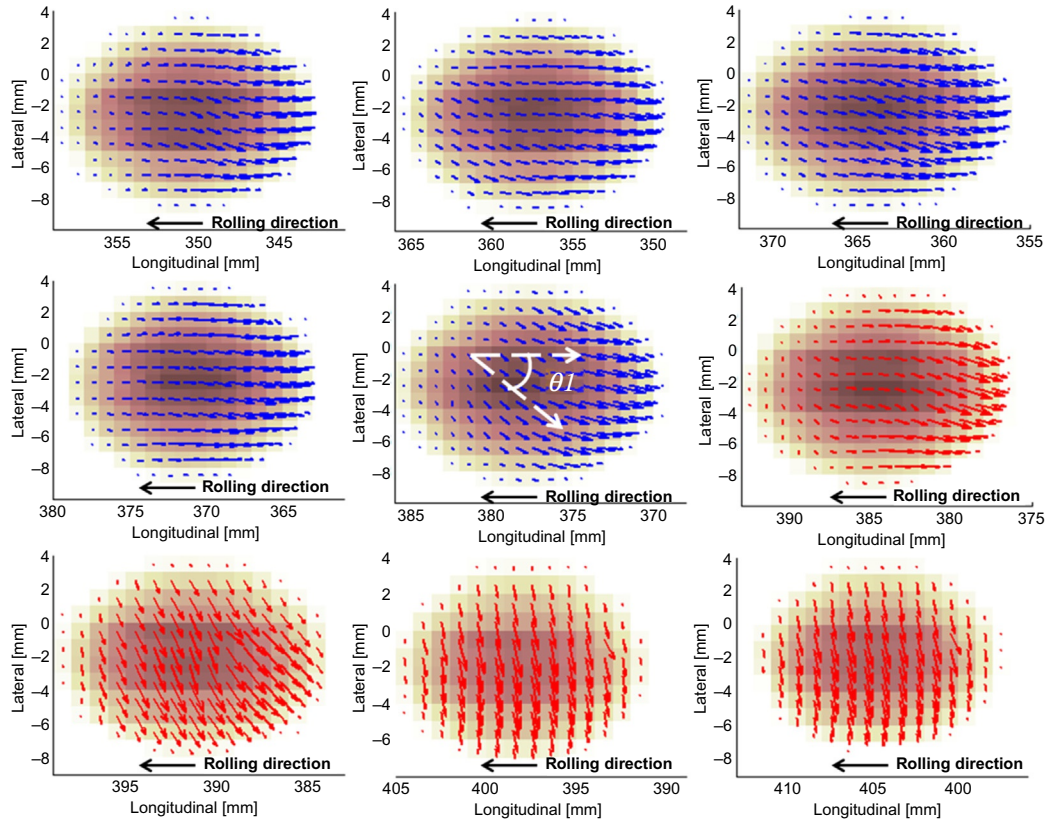**Fig. 7.11** Evolution of pressure and surface shear stress distributions in Patch 2 (*red color* (*dark gray* in print version) for shear stress indicates two-point contact).

Reproduced with permission from Z. Yang, Z.L. Li, R. Dollevoet, Modelling of non-steady-state transition from single-point to two-point rolling contact, Tribol. Int. 101 (2016) 152–163, https://doi.org/10.1016/j.triboint.2016.04.023.
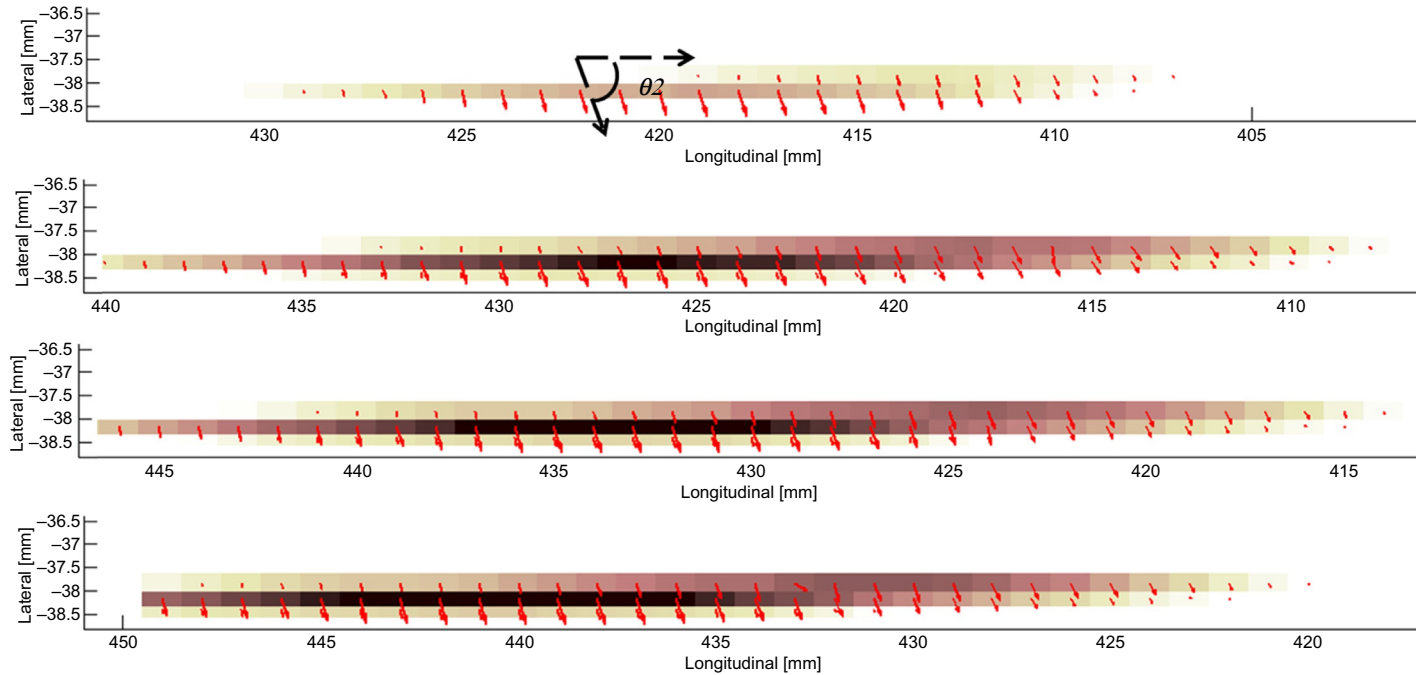
participation of the 2nd contact patch increases. $\theta2$ changes only slightly from the first occurrence of Patch 2 onwards. Detailed analyses of contact solutions during the nonsteady-state transition, including the contact-induced waves, can be found in [40].

7.2.3 Waves induced by wheel-rail dynamic interaction

Contact-induced waves inherently exist in the wheel-rail dynamic interaction. With the explicit FE modeling of dynamic interaction, the wheel-rail contact-induced waves were reproduced by the three aforementioned examples. According to the generation mechanism, the waves are categorized as the impact-induced wave, large-creepage-induced wave, and perturbation-induced wave. See [42] for the descriptions of the three types of waves. The generation mechanisms of the former two are evident: the significant dynamic effect or kinetic energy [44] induced by the wheel-rail impact or large creepage results in large oscillations of the wheel/rail surface material particles in the vicinity of the contact patch; the large local oscillations then propagate and form regular wave patterns.

The perturbation arises during seemingly steady-state rolling. The initiation of the perturbation has been found either close to the leading edge of the contact patch or at the juncture of the adhesion-slip regions, where the surface shear stress is close, but not equal, to the traction bound; therefore, the contacting particles originally in adhesion at these locations are more likely to slip than those elsewhere with an increase of the surface shear stress or a decrease of the contact pressure. Because the variation in the stress distribution is caused by vibration [45], the perturbation-induced waves are intrinsically generated by dynamic effects similar to the impact-induced wave and the creepage-induced wave. In addition, the perturbation-induced waves are found to generally initiate at the leading edge of the contact patch in the wheel braking condition, whereas the waves are initiated more often at the juncture of the adhesion-slip regions in wheel traction conditions.

The physical characteristics of the wheel-rail contact-induced waves can be revealed by analyzing the nodal motion on the contact surface that forms the wave. A typical large-creepage-induced wave is analyzed in [42]. The nodal velocities are narrow-banded signals and have a dominant frequency around 0.495 MHz. By multiplying the wavelength and the frequency of nodal velocity, the wave speed can be calculated, which is about 3 km/s. In addition, the phases out of the tangential and normal nodal velocities are approximately $\pi/2$. These characteristics correspond to the simulated large-creepage-induced wave to Rayleigh wave.

Experimental investigations [46,47] have suggested that Rayleigh waves can be used to detect rail cracks. The successful reproduction of the Rayleigh wave qualifies the explicit FEM for the simulation of crack-induced waves, which may contribute to the early-stage detection of cracks in the rail surface. Fig. 7.12A and B shows the distribution of the rail surface nodal velocities within the whole solution zone when the wheel was approaching and rolling over the crack in the simulation, respectively. The contact patch is indicated by the dashed black oval; the crack is denoted by the thick black line. The wave patterns observed in Fig. 7.12 were generated at the location of the crack and propagated radially. The wave generated when the wheel was rolling
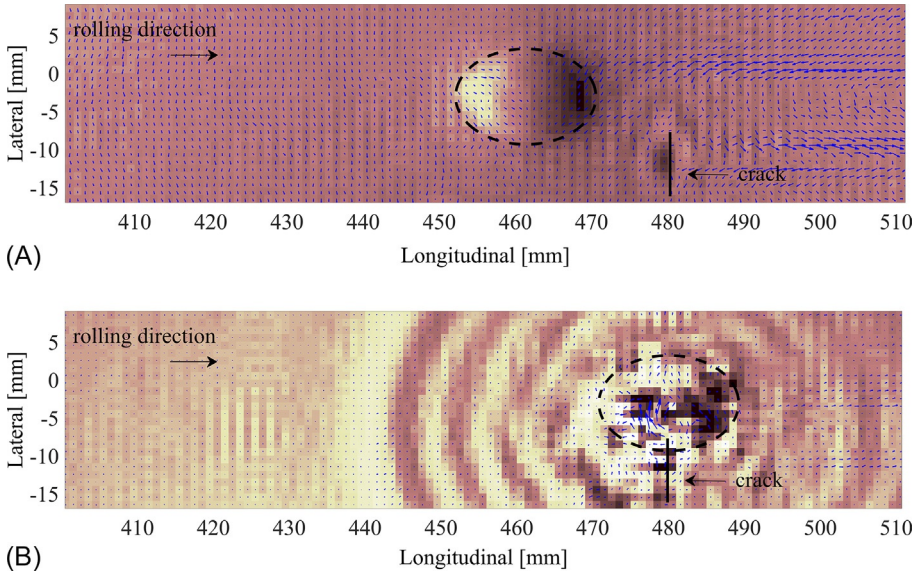
Fig. 7.12 Contact-induced waves influenced by a crack (A) wheel approaches the crack; (B) wheel rolls over the crack.

over the crack is more significant than the wave generated when the wheel was approaching the crack. See [42] for the simulation model and more detailed results analyses.

7.3   Detection and maintenance

7.3.1   Detection of wheel-rail dynamic interaction-related problems

Because wheel-rail dynamic interaction generates high-amplitude wheel-rail contact force and structural vibration, the related problems, i.e., wheel/track structural degradation, vibration, and noise radiation can be detected with the measurements of wheel-rail contact force, wheel, and track vibration. Hardly can the vibration of rolling wheels be directly measured. Alternatively, axle box acceleration (ABA) measurement has been used extensively to quantify the wheel axle responses and to identify the wheel-rail dynamic interaction-related problems [48–53]. Note that here the discussion is about the detection techniques based on the responses of wheel-rail dynamic interaction; therefore, the detection methods such as ultrasonic measurements, eddy current testing, image recognition are not included.

7.3.1.1   Detection with the contact force measurement

Wheel-rail contact force can be measured with track-side or/and wheelset instrumentation of strain gauge. The wheel-rail contact force up to 2 kHz can be obtained with the strain gauge measurement [54]. Track-side measurements are generally employed when the condition of a certain section of the track, usually a weak spot, needs to be monitored. Fig. 7.13 shows an example of the strain gauge instrumentation.

The large contact force can be correlated to several types of track/wheel degradations such as bad rail joints, wheel flats, corrugations, and fastening failure. The dynamic load factor, i.e., the ratio between the dynamic force and the static/nominal load, has been widely used to estimate the track [55] and wheel conditions [56,57]. In addition, the adhesion condition (i.e., traction of wheels to accelerate and brake) and climb index (i.e., L/V ratio) at curves can be evaluated based on the measured force signals. The strain gauge instrumented wheelset can efficiently measure the wheel-rail contact force along a railway line, which is suitable for wide-scale track condition monitoring and detection of different classes of rail irregularities [54].

7.3.1.2   Detection with the ABA measurement

ABA measurements have been employed to detect track defects such as corrugation, welds, squats, poor-quality joints, and turnouts [48–53]. A train-borne ABA measurement system is schematically shown in Fig. 7.14, which offers the following advantages [50]:

- ABA is a low-cost measurement system compared to other types of detection methods.
- The sensors are easy to maintain.
- ABA can be implemented on in-service operational trains.
- Early rail defects are possibly detected with no need for expensive and complex instrumentation.
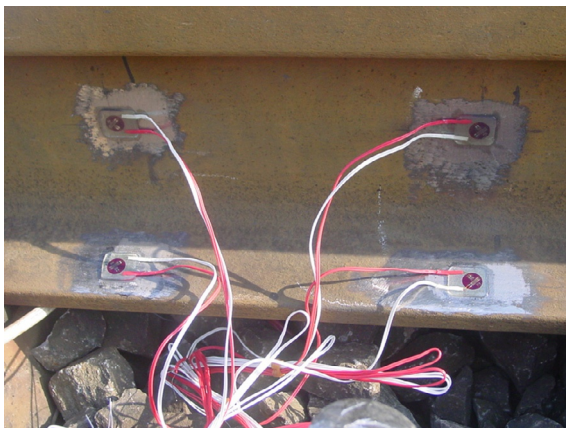- The ABA signals can reflect the severity level of the dynamic contact force.

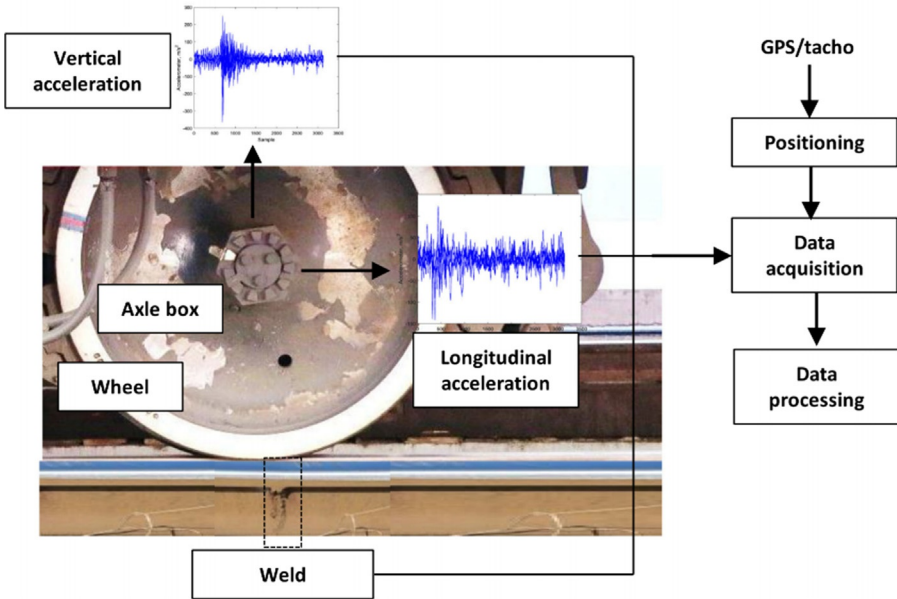**Fig. 7.13** Strain gauges instrumentation.

Fig. 7.14 Train-borne ABA measurement system.
Reproduced from A. Nunez, A. Jamshidi, H. Wang, Pareto-based maintenance decisions for
regional railways with uncertain weld conditions using the Hilbert spectrum of axle
box acceleration, IEEE Trans. Ind. Inf. 15 (2019) 1496–1507, https://doi.org/10.1109/tii.2018.
2847736, open source.

The ABA measurements can have some drawbacks [43]: First, when the wheel is dam-
aged, the ABA signals and the assessment of rail irregularities are affected by vibra-
tion originated from the wheel; this can be overcome with proper instrumentation and
signal processing [48,58]. Second, ABA measurements are speed-dependent. To elim-
inate the influence of the train speed, the measurements should be performed at a con-
stant speed, and were not possible, a mapping between ABA measurements and speed
is needed. Thirdly, the frequencies of track vibration are dependent on the stiffness
and damping properties of the track. This needs to be considered especially when
the detected railway line consists of different tracks (e.g., ballast and nonballast).

7.3.1.3   Detection with the track vibration measurement

Track vibration is often measured with controlled excitations, e.g., by hammers
[59,60] or falling weights [61,62], or under dynamic train, loading using specialized
measurement vehicles [63] or operational trains [39]. Hammer tests are broadly used
to measure the frequency response functions of track structures. The frequency
response functions, on one hand, reflect the track structural dynamic behavior (i.e.,
the modal frequency, modal shape, and damping ratio) and thus healthy conditions

in terms of dynamics, and on the other, can be used to derive the parameters of the track components, e.g., the support stiffness and damping [59]. Since the support stiffness and damping of the track needs to be identified in the ABA and train pass-by measurements, hammer tests are sometimes conducted as supplements to the ABA and train pass-by detection.

Track vibration in the low-frequency range (below 150 Hz) corresponds mainly to the dynamics of the substructure components (i.e., subgrade and ballast) [64]. To fully excite these components, the falling weight test is a good option to provide sufficient energy. The track vibration at 150–800 Hz is closely related to the rails and track superstructure components (i.e., fastening, railpad, and sleeper), the vibration in this frequency range is best tested using a sledgehammer with a soft tip [65]. At higher frequencies (800–5000 Hz), track vibration is dominated by the rails, and a light hammer with a hard tip should be used [39].

Track vibration induced by passing trains can be measured to assess the condition of a certain section of track, usually a weak spot [61]. Passing trains can excite tracks to vibrate in a wide frequency range, e.g., up to 10 kHz when impacts occur at an IRJ [39]. In combination with a hammer test, the resonances of the track structure contributing greatly to the impact vibration at the IRJ can be identified: the rail resonance (rail mass on the fastening stiffness [66]) and the pinned-pinned resonance.

7.3.2 Maintenance of weak spots of the track

Timely maintenance can prevent failures of track components and traffic disruptions and minimize the life cycle cost of the railway infrastructure. The failures of track components caused by wheel-rail dynamic interaction occur mainly at weak spots of the track. This section briefly discusses the maintenance of the track weak spots, i.e., the impact-inducing track sections and large-friction-inducing sections.

7.3.2.1 Maintenance of the impact-inducing track sections

Because wheel-rail impacts are caused by stiffness or/and geometric irregularities of railway tracks, the countermeasures against impact may be divided into stiffness control and geometric control. Taking the joints as an example, the dynamic stiffness at joints can be controlled by ballast maintenance and optimizing the sleeper set-up and distribution. Ballast tamping and renewal mitigates the track irregularities in both stiffness and geometry. To reduce the deflection of the joint, two commonly used sleeper set-ups are the suspended rail joint (with the joint between two adjacent sleepers) and the supported rail joint (one sleeper right beneath the joint). A conceptual design, termed as embedded IRJ was presented in [67], in which the rails were embedded into the concrete of the posttensioned sleepers. The numerical simulations indicate that the performance of the embedded IRJ is superior under wheel-rail impacts. An experimental study [68] conducted in the Dutch railway indicates that the amplitude of the rail resonance decreases with the 1st sleeper span after the joint, whereas the amplitude of the pinned-pinned resonance decreases with the difference

between the 1st and 2nd sleeper spans. The nonuniform sleeper distribution at the IRJ is thus proposed to reduce wheel-rail impacts at IRJs.

As to the geometric control, timely grinding is an effective way to reduce wheel-rail impact force. As reported in [17], the numerically simulated wheel-rail contact force increases from 130 kN (quasistatic load) to 160 kN at a new joint (with nominal rail profile), and to 230 kN at a worn joint (with measured rail profile). In addition, antiimpact rail profiles [69–71] have been proposed for the rail joint and turnout sections.

At turnouts, the grinding-welding-grinding method can be performed to control the wheel-rail contact geometry and to extend the service life. First, the crossing rails were ground to remove surface damage (e.g., cracks, uneven wear, and plastic deformation); second, the hollow regions caused by the grinding were filled by welding; finally, the crossing rails were ground again to the desired profiles [53]. The repair was performed manually because the train-borne grinding machine is incapable of operating at the turnout section.

7.3.2.2 Maintenance of the large-friction-inducing sections

A straightforward way to maintain the large-friction-inducing sections is to manage wheel-rail friction. A low coefficient of friction (COF) is desired to reduce rail wear (especially at shape curves [72]), head checks (HCs) [73], noise [74], and energy consumption of railway transportation [75]. However, low COFs may result in low adhesion, which then generates severe rail burn and wheel flat, affects punctuality in traction operation, and threaten safety during braking. To guarantee the safe acceleration and braking which has maximum demand for COF, the required COFs are 0.25 in traction and 0.14 in braking in the Dutch railway [76]. The COF required in traction is larger because a considerably lower number of wheel axles is involved in the acceleration than in braking.

Friction modifiers (FMs) can be applied to the wheel-rail interface either by trackside or train-borne installations. However, providing a proper dosage of the FMs is challenging because it varies case by case, influenced by weather and characteristics of the FMs, etc. Smaller quantities of FMs do not provide a stable level of adhesion and the lasting effects are limited, whereas bigger quantities have a longer-lasting effect, but critically low adhesion levels may be caused after the application of FMs.

Grinding is a commonly used approach for the maintenance of the large-friction-inducing sections to restore the rail profile and to remove RCF cracks. The best treatment available for HCs and corrugation would be early detection and removal by grinding. In addition, rail profile optimization can effectively prevent or retard HC initiation. The anti-HC profile presented in [77] has been normalized as a standard European rail profile. By avoiding contact in the HC-prone part of the rail, the maximum surface shear stress is greatly reduced, mainly owing to the decrease of spin in the contact. Large-scale application of the anti-HC profile on the Dutch railway network shows that HCs in 2008 were reduced by about 70% with respect to 2004 when HC was the most widespread.

References

[1] H. Hertz, Ueber die Berührung fester elastischer Körper, J. Reine Angew. Math. 1882 (1882), https://doi.org/10.1515/crll.1882.92.156.

[2] R.D. Mindlin, Compliance of elastic bodies in contact, J. Appl. Mech. 16 (3) (1949) 259–268.

[3] F.W. Carter, On the action of a locomotive driving wheel, P. R. Soc. Lond. A 112 (1926) 151–157, https://doi.org/10.1098/rspa.1926.0100.

[4] P.J. Vermeulen, K.L. Johnson, Contact of nonspherical elastic bodies transmitting tangential forces, J. Appl. Mech. 31 (1964) 338, https://doi.org/10.1115/1.3629610.

[5] J.J. Kalker, Three-Dimensional Elastic Bodies in Rolling Contact, first ed., Springer, The Netherlands, 1990.

[6] J. Ringsberg, Rolling contact fatigue analysis of rails inculding numerical simulations of the rail manufacturing process and repeated wheel-rail contact loads, Int. J. Fatigue 25 (2003) 547–558, https://doi.org/10.1016/s0142-1123(02)00147-0.

[7] T. Telliskivi, U. Olofsson, Wheel–rail wear simulation, Wear 257 (2004) 1145–1153, https://doi.org/10.1016/j.wear.2004.07.017.

[8] A. Sladkowski, M. Sitarz, Analysis of wheel–rail interaction using FE software, Wear 258 (2005) 1217–1223, https://doi.org/10.1016/j.wear.2004.03.032.

[9] M. Wiest, E. Kassa, W. Daves, J.C.O. Nielsen, H. Ossberger, Assessment of methods for calculating contact pressure in wheel-rail/switch contact, Wear 265 (2008) 1439–1445, https://doi.org/10.1016/j.wear.2008.02.039.

[10] Z. Li, X. Zhao, C. Esveld, R. Dollevoet, M. Molodova, An investigation into the causes of squats—correlation analysis and numerical modeling, Wear 265 (2008) 1349–1355, https://doi.org/10.1016/j.wear.2008.02.037.

[11] A. Ekberg, J. Sandström, Numerical study of the mechanical deterioration of insulated rail joints, Proc. Inst. Mech. Eng. F J. Rail Rapid Transit 223 (2009) 265–273, https://doi.org/10.1243/09544097jrrt243.

[12] A. Johansson, B. Pålsson, M. Ekh, J.C.O. Nielsen, M.K.A. Ander, J. Brouzoulis, E. Kassa, Simulation of wheel–rail contact and damage in switches & crossings, Wear 271 (2011) 472–481, https://doi.org/10.1016/j.wear.2010.10.014.

[13] X. Zhao, Z.L. Li, The solution of frictional wheel-rail rolling contact with a 3D transient finite element model: validation and error analysis, Wear 271 (2011) 444–452, https://doi.org/10.1016/j.wear.2010.10.007.

[14] Z. Li, R. Dollevoet, M. Molodova, X. Zhao, Squat growth—some observations and the validation of numerical predictions, Wear 271 (2011) 148–157, https://doi.org/10.1016/j.wear.2010.10.051.

[15] X. Zhao, Z.L. Li, A three-dimensional finite element solution of frictional wheel-rail rolling contact in elasto-plasticity, Proc. Inst. Mech. Eng. B J. Eng. 229 (2015) 86–100, https://doi.org/10.1177/1350650114543717.

[16] Z. Wei, C. Shen, Z. Li, R. Dollevoet, Wheel–rail impact at crossings: relating dynamic frictional contact to degradation, J. Comput. Nonlinear Dyn. 12 (2017), https://doi.org/10.1115/1.4035823, 041016.

[17] Z. Yang, A. Boogaard, Z. Wei, J. Liu, R. Dollevoet, Z. Li, Numerical study of wheel-rail impact contact solutions at an insulated rail joint, Int. J. Mech. Sci. 138–139 (2018) 310–322, https://doi.org/10.1016/j.ijmecsci.2018.02.025.

[18] Z. Yang, X. Deng, Z. Li, Numerical modeling of dynamic frictional rolling contact with an explicit finite element method, Tribol. Int. 129 (2019) 214–231, https://doi.org/10.1016/j.triboint.2018.08.028.

[19] X. Deng, Z. Li, Z. Qian, W. Zhai, Q. Xiao, R. Dollevoet, Pre-cracking development of weld-induced squats due to plastic deformation: five-year field monitoring and numerical analysis, Int. J. Fatigue 127 (2019) 431–444, https://doi.org/10.1016/j.ijfatigue.2019.06.013.

[20] Z. Li, J.J. Kalker, Simulation of severe wheel-rail wear, in: Proceedings of the 6th International Conference on Computer Aided Design, Manufacture and Operation in the Railway and Other Advanced Mass Transit Systems, Lisbon, Portugal, 1998, pp. 393–402, https://doi.org/10.2495/CR980381.

[21] Y. Wu, X. Du, H.-J. Zhang, Z.-F. Wen, X.-S. Jin, Experimental analysis of the mechanism of high-order polygonal wear of wheels of a high-speed train, J. Zhejiang Univ. Sci. A 18 (2017) 579–592, https://doi.org/10.1631/jzus.A1600741.

[22] G. Tao, Z. Wen, X. Liang, D. Ren, X. Jin, An investigation into the mechanism of the out-of-round wheels of metro train and its mitigation measures, Veh. Syst. Dyn. 57 (2018) 1–16, https://doi.org/10.1080/00423114.2018.1445269.

[23] W. Cai, M. Chi, X. Wu, F. Li, Z. Wen, S. Liang, X. Jin, Experimental and numerical analysis of the polygonal wear of high-speed trains, Wear 440–441 (2019), https://doi.org/10.1016/j.wear.2019.203079.

[24] X. Deng, Z. Qian, Z. Li, R. Dollevoet, Investigation of the formation of corrugation-induced rail squats based on extensive field monitoring, Int. J. Fatigue 112 (2018) 94–105, https://doi.org/10.1016/j.ijfatigue.2018.03.002.

[25] R. Dollevoet, Z. Li, O. Arias-Cuevas, A method for the prediction of head checking initiation location and orientation under operational loading conditions, Proc. Inst. Mech. Eng. F J. Rail Rapid Transit 224 (2010) 369–374, https://doi.org/10.1243/09544097jrrt368.

[26] A. Zoeteman, R. Dollevoet, Z. Li, Dutch research results on wheel/rail interface management: 2001–2013 and beyond, Proc. Inst. Mech. Eng. F J. Rail Rapid Transit 228 (2014) 642–651, https://doi.org/10.1177/0954409714524379.

[27] S.L. Grassie, Rail corrugation: characteristics, causes, and treatments, Proc. Inst. Mech. Eng. F J. Rail Rapid Transit 223 (2009) 581–596, https://doi.org/10.1243/09544097jrrt264.

[28] S. Li, Z. Li, A. Núñez, R. Dollevoet, New insights into the short pitch corrugation enigma based on 3D-FE coupled dynamic vehicle-track modeling of frictional rolling contact, Appl. Sci. 7 (2017) 807, https://doi.org/10.3390/app7080807.

[29] D.J. Thompson, Railway Noise and Vibration: Mechanisms, Modelling and Means of Control, Elsevier, 2009.

[30] Z.Y. Huang, D.J. Thompson, C.J.C. Jones, Squeal prediction for a bogied vehicle in a curve, Notes Numer. Fluid Mech. 99 (2008) 313–319, https://doi.org/10.1007/978-3-540-74893-9_44.

[31] Z. Yang, Z. Li, Numerical modeling of wheel-rail squeal-exciting contact, Int. J. Mech. Sci. 153–154 (2019) 490–499, https://doi.org/10.1016/j.ijmecsci.2019.02.012.

[32] Z.L. Li, X. Zhao, R. Dollevoet, M. Molodova, Differential wear and plastic deformation as causes of squat at track local stiffness change combined with other track short defects, Veh. Syst. Dyn. 46 (2008) 237–246, https://doi.org/10.1080/00423110801935855.

[33] X. Zhao, Z. Li, A solution of transient rolling contact with velocity dependent friction by the explicit finite element method, Eng. Comput. 33 (2016) 1033–1050, https://doi.org/10.1108/ec-09-2014-0180.

[34] X. Zhao, X.G. Zhao, C. Liu, Z.F. Wen, X.S. Jin, A study on dynamic stress intensity factors of rail cracks at high speeds by a 3D explicit finite element model of rolling contact, Wear 366 (2016) 60–70, https://doi.org/10.1016/j.wear.2016.06.001.

[35] M. Pletz, W. Daves, H. Ossberger, A wheel set/crossing model regarding impact, sliding and deformation-explicit finite element approach, Wear 294 (2012) 446–456, https://doi.org/10.1016/j.wear.2012.07.033.

[36] D.M. Mulvihill, M.E. Kartal, D. Nowell, D.A. Hills, An elastic–plastic asperity interaction model for sliding friction, Tribol. Int. 44 (2011) 1679–1694, https://doi.org/10.1016/j.triboint.2011.06.018.

[37] P. Wriggers, Computational Contact Mechanics, Springer, Berlin Heidelberg, 2006.

[38] G. Noh, K.-J. Bathe, An explicit time integration scheme for the analysis of wave propagations, Comput. Struct. 129 (2013) 178–193, https://doi.org/10.1016/j.compstruc.2013.06.007.

[39] Z. Yang, A. Boogaard, R. Chen, R. Dollevoet, Z. Li, Numerical and experimental study of wheel-rail impact vibration and noise generated at an insulated rail joint, Int. J. Impact Eng. 113 (2018) 29–39, https://doi.org/10.1016/j.ijimpeng.2017.11.008.

[40] Z. Yang, Z.L. Li, R. Dollevoet, Modelling of non-steady-state transition from single-point to two-point rolling contact, Tribol. Int. 101 (2016) 152–163, https://doi.org/10.1016/j.triboint.2016.04.023.

[41] I. Zenzerovic, W. Kropp, A. Pieringer, An engineering time-domain model for curve squeal: tangential point-contact model and Green's functions approach, J. Sound Vib. 376 (2016) 149–165, https://doi.org/10.1016/j.jsv.2016.04.037.

[42] Z. Yang, Z. Li, A numerical study on waves induced by wheel-rail contact, Int. J. Mech. Sci. 161–162 (2019), https://doi.org/10.1016/j.ijmecsci.2019.105069, 105069.

[43] D.J. Thompson, G. Squicciarini, B. Ding, L. Baeza, A state-of-the-art review of curve squeal noise: phenomena, mechanisms, modelling and mitigation, in: Notes on Numerical Fluid Mechanics and Multidisciplinary Design, 139, Springer, 2018, pp. 3–41, https://doi.org/10.1007/978-3-319-73411-8_1.

[44] J. Reed, Energy-losses due to elastic wave-propagation during an elastic impact, J. Phys. D Appl. Phys. 18 (1985) 2329–2337, https://doi.org/10.1088/0022-3727/18/12/004.

[45] H. Ouyang, W. Nack, Y. Yuan, F. Chen, Numerical analysis of automotive disc brake squeal: a review, Int. J. Veh. Noise Vib. 1 (2005) 207, https://doi.org/10.1504/ijvnv.2005.007524.

[46] P.R. Armitage, The use of low-frequency Rayleigh waves to detect gauge corner cracking in railway lines, Insight 44 (2002) 369–372.

[47] A. Pantano, D. Cerniglia, Simulation of laser generated ultrasound with application to defect detection, Appl. Phys. A 91 (2008) 521–528, https://doi.org/10.1007/s00339-008-4442-1.

[48] M. Molodova, Z. Li, A. Nunez, R. Dollevoet, Automatic detection of squats in railway infrastructure, IEEE Trans. Intell. Transp. Syst. 15 (2014) 1980–1990, https://doi.org/10.1109/tits.2014.2307955.

[49] M. Oregui, S. Li, A. Núñez, Z. Li, R. Carroll, R. Dollevoet, Monitoring bolt tightness of rail joints using axle box acceleration measurements, Struct. Control. Health Monit. 24 (2017), https://doi.org/10.1002/stc.1848.

[50] A. Nunez, A. Jamshidi, H. Wang, Pareto-based maintenance decisions for regional railways with uncertain weld conditions using the Hilbert spectrum of axle box acceleration, IEEE Trans. Ind. Inf. 15 (2019) 1496–1507, https://doi.org/10.1109/tii.2018.2847736.

[51] P.F. Westeon, C.S. Ling, C. Roberts, C.J. Goodman, P. Li, R.M. Goodall, Monitoring vertical track irregularity from in-service railway vehicles, Proc. Inst. Mech. Eng. F J. Rail Rapid Transit 221 (2016) 75–88, https://doi.org/10.1243/0954409jrrt65.

[52] A.M. Remennikov, S. Kaewunruen, A review of loading conditions for railway track structures due to train and track vertical interaction, Struct. Control. Health Monit. 15 (2008) 207–234, https://doi.org/10.1002/stc.227.

[53] Z. Wei, A. Núñez, Z. Li, R. Dollevoet, Evaluating degradation at railway crossings using axle box acceleration measurements, Sensors 17 (2017), https://doi.org/10.3390/s17102236.

[54] P. Gullers, L. Andersson, R. Lundén, High-frequency vertical wheel–rail contact forces—field measurements and influence of track irregularities, Wear 265 (2008) 1472–1478, https://doi.org/10.1016/j.wear.2008.02.035.

[55] J.R. Edwards, A. Cook, M.S. Dersch, Y. Qian, Quantification of rail transit wheel loads and development of improved dynamic and impact loading factors for design, Proc. Inst. Mech. Eng. F J. Rail Rapid Transit 232 (2018) 2406–2417, https://doi.org/10.1177/0954409718770924.

[56] B. Stratman, Y. Liu, S. Mahadevan, Structural health monitoring of railroad wheels using wheel impact load detectors, J. Fail. Anal. Prev. 7 (2007) 218–225, https://doi.org/10.1007/s11668-007-9043-3.

[57] A. Alemi, Railway Wheel Defect Identification (Ph.D. thesis), Delft University of Technology, 2019.

[58] Z. Li, M. Molodova, A. Nunez, R. Dollevoet, Improvements in axle box acceleration measurements for the detection of light squats in railway infrastructure, IEEE Trans. Ind. Electron. 62 (2015) 4385–4397, https://doi.org/10.1109/tie.2015.2389761.

[59] M. Oregui, Z. Li, R. Dollevoet, Identification of characteristic frequencies of damaged railway tracks using field hammer test measurements, Mech. Syst. Signal Process. 54–55 (2015) 224–242, https://doi.org/10.1016/j.ymssp.2014.08.024.

[60] S. Kaewunruen, A.M. Remennikov, Field trials for dynamic characteristics of railway track and its components using impact excitation technique, NDT&E Int. 40 (2007) 510–519, https://doi.org/10.1016/j.ndteint.2007.03.004.

[61] M.P.N. Burrow, A.H.C. Chan, A. Shein, Deflectometer-based analysis of ballasted railway tracks, Proc. Inst. Civ. Eng. Geotech. Eng. 160 (2007) 169–177, https://doi.org/10.1680/geng.2007.160.3.169.

[62] S. Kaewunruen, A.M. Remennikov, Progressive failure of prestressed concrete sleepers under multiple high-intensity impact loads, Eng. Struct. 31 (2009) 2460–2473, https://doi.org/10.1016/j.engstruct.2009.06.002.

[63] E.G. Berggren, A. Nissen, B.S. Paulsson, Track deflection and stiffness measurements from a track recording car, Proc. Inst. Mech. Eng. F J. Rail Rapid Transit 228 (2014) 570–580, https://doi.org/10.1177/0954409714529267.

[64] K. Knothe, Y. Wu, Receptance behaviour of railway track and subgrade, Arch. Appl. Mech. 68 (1998) 457–470, https://doi.org/10.1007/s004190050179.

[65] Z. Wei, A. Boogaard, A. Nunez, Z. Li, R. Dollevoet, An integrated approach for characterizing the dynamic behavior of the wheel–rail interaction at crossings, IEEE Trans. Instrum. Meas. 67 (2018) 2332–2344, https://doi.org/10.1109/tim.2018.2816800.

[66] N. Vincent, D.J. Thompson, Track dynamic behaviour at high frequencies. Part 2: Experimental results and comparisons with theory, Veh. Syst. Dyn. 24 (1995) 100–114, https://doi.org/10.1080/00423119508969618.

[67] N. Zong, M. Dhanasekar, Sleeper embedded insulated rail joints for minimising the number of modes of failure, Eng. Fail. Anal. 76 (2017) 27–43, https://doi.org/10.1016/j.engfailanal.2017.02.001.

[68] I. Papaioannou, Experimental and Numerical Study on the Optimisation of Insulated Rail Joint Dynamic Behaviour (M.Sc. thesis), Delft University of Technology, 2018.

[69] R.H. Plaut, H. Lohse-Busch, A. Eckstein, S. Lambrecht, D.A. Dillard, Analysis of tapered, adhesively bonded, insulated rail joints, Proc. Inst. Mech. Eng. F J. Rail Rapid Transit 221 (2007) 195–204, https://doi.org/10.1243/0954409jrrt107.

[70] C. Wan, V. Markine, R. Dollevoet, Robust optimisation of railway crossing geometry, Veh. Syst. Dyn. 54 (2016) 617–637, https://doi.org/10.1080/00423114.2016.1150495.

[71] C. Wan, V.L. Markine, I.Y. Shevtsov, Improvement of vehicle–turnout interaction by optimising the shape of crossing nose, Veh. Syst. Dyn. 52 (2014) 1517–1540, https://doi.org/10.1080/00423114.2014.944870.

[72] X. Lu, T.W. Makowsky, D.T. Eadie, K. Oldknow, J. Xue, J. Jia, G. Li, X. Meng, Y. Xu, Y. Zhou, Friction management on a Chinese heavy haul coal line, Proc. Inst. Mech. Eng. F J. Rail Rapid Transit 226 (2012) 630–640, https://doi.org/10.1177/0954409712447170.

[73] R. Stock, D.T. Eadie, D. Elvidge, K. Oldknow, Influencing rolling contact fatigue through top of rail friction modifier application – a full scale wheel–rail test rig study, Wear 271 (2011) 134–142, https://doi.org/10.1016/j.wear.2010.10.006.

[74] D.T. Eadie, M. Santoro, J. Kalousek, Railway noise and the effect of top of rail liquid friction modifiers: changes in sound and vibration spectral distributions in curves, Wear 258 (2005) 1148–1155, https://doi.org/10.1016/j.wear.2004.03.061.

[75] G. Idárraga Alarcón, N. Burgelman, J.M. Meza, A. Toro, Z. Li, The influence of rail lubrication on energy dissipation in the wheel/rail contact: a comparison of simulation results with field measurements, Wear 330–331 (2015) 533–539, https://doi.org/10.1016/j.wear.2015.01.008.

[76] O. Arias-Cuevas, Z. Li, Field investigations into the adhesion recovery in leaf-contaminated wheel–rail contacts with locomotive sanders, Proc. Inst. Mech. Eng. F J. Rail Rapid Transit 225 (2011) 443–456, https://doi.org/10.1177/2041301710394921.

[77] R.P.B.J. Dollevoet, Design of an Anti Head Check Profile Based on Stress Relief (Ph.D. thesis), University of Twente, 2010.